RESEARCH ARTICLE

Check for updates

Universal synthesis of coral-like ternary MOF-derived sulfides as efficient OER electrocatalysts†

Tianpeng Liu,[a] Yangping Zhang,[a] Jun Yu,[a] Mengyun Hu,[a] Zhengying Wu, ⓘ *[b] Xiao Wei,[a] Shudi Yu[a] and Yukou Du ⓘ *[a]

The strategy of synthesizing high-efficiency oxygen evolution reaction (OER) catalysts using sacrificing metal–organic framework (MOF) templates is considered promising. However, few reports have focused on improving the intrinsic electrocatalytic activity of the MOF templates. Herein, we have developed a universal synthesis method for synthesizing a series of ternary coral-like FeNiM (M = Zn, Co and Cd) MOF templates. Benefitting from the synergistic effect, these trimetallic templates exhibit identical morphologies and outstanding OER performance compared to mono-metal templates. Moreover, transition metal sulfides (FeNiZnS) have been synthesized to enhance the overall electrical conductivity of catalyst materials. Optimized FeNiZnS-1 exhibits a minimal overpotential of 249 mV to achieve a current density of 10 mA cm^{-2}, alongside outstanding electrochemical durability over 60 h in chronopotentiometry (CP) testing. The two-electrode couple FeNiZnS-1//Pt/C achieves a cell voltage of 1.54 V at 10 mA cm^{-2} for overall water splitting in 1 M KOH solution.

Introduction

Climate deterioration has intensified the global demand for a new energy revolution. The development of renewable and non-polluting new green energy and storage modes has achieved consensus among governments worldwide.[1,2] Clean energy sources such as hydrogen, wind, hydropower, and solar power hold promise as viable alternatives for traditional fossil energy. Hydrogen not only has the highest energy density found in fuels, but also serves as an effective form of energy storage, reducing the wastage of other clean energy.[3] Hydrogen can be classified into three categories based on its production process: green hydrogen, grey hydrogen, and blue hydrogen.[4,5] Among these, green hydrogen has attracted significant attention due to its minimal environmental pollution during production. Compared to the photoelectrochemical water splitting, the electrolysis of water for green hydrogen production has achieved initial industrialization with a higher energy con-

*[a]College of Chemistry, Chemical Engineering and Materials Science, Soochow University, Industrial Park, Renai Road, Suzhou 215123, PR China.
E-mail: duyk@suda.edu.cn*
[b]Jiangsu Key Laboratory for Environment Functional Materials, School of Materials Science and Engineering, Suzhou University of Science and Technology, Suzhou 215009, China. E-mail: zywu@mail.usts.edu.cn
†Electronic supplementary information (ESI) available. See DOI: https://doi.org/10.1039/d4qi01725k

version efficiency.[6,7] However, the sluggish kinetics of the anodic half-reaction (oxygen evolution reaction, OER) has resulted in a high overpotential in the overall water splitting.[8,9] Numerous catalytic materials have been developed to reduce the overpotential of the OER. Noble metal oxides (such as IrO_2 and RuO_2) demonstrate superior catalytic performance compared to transition metal-based electrocatalysts.[10,11] But the rare sources and high cost restrict the widespread application of noble metal-based catalytic materials. Therefore, balancing the cost and performance of catalytic materials is key to solving the high overpotential issue in water splitting.

The multifunctional porous materials, metal–organic frameworks (MOF), have been widely employed in the field of electrocatalysis over the past two decades.[12–14] Due to their intrinsic low electrical conductivity, pristine MOFs are not directly used as OER electrocatalysts.[15] However, utilizing pristine MOFs as templates or sacrificing precursor materials for the synthesis of MOF-derived electrocatalysts (metal phosphides, metal sulphides, and metal oxides) possesses remarkable advantages.[16–19] Benefiting from the diverse chemical compositions and structures, converting pristine MOFs into MOF-derived electrocatalysts can significantly enhance the electrocatalytic performance of the materials. The OER performance of classic MOF templates (such as ZIF8, ZIF67 and MIL53) is often limited by their mono-metal active sites and poor conductivity.[20,21] Conventional optimization strategies mainly aim to transform templates into MOF-derived catalysts,

6064 | *Inorg. Chem. Front.*, 2024, **11**, 6064–6071

This journal is © the Partner Organisations 2024

with few researchers focusing on enhancing the intrinsic performance of MOF templates.[22] MOF-derived sulphides inherit the inherent advantages of high specific surface area and high porosity.[23–25] Furthermore, the organic ligands transform into carbon frameworks during high-temperature sulfidation, enhancing the conductivity of the material and facilitating electron transfer in electrochemical reactions.[26,27] Unfortunately, during the hydrothermal sulfidation process, the morphology of MOF templates is susceptible to being destroyed, resulting in a low electrocatalytic performance.[28,29] Thus, it is necessary to intricately regulate the reaction time and temperature in order to achieve preservation of the MOF morphology.

In this work, we have developed a universal synthetic strategy and successfully synthesized a series of coral-like ternary MOF templates. Benefitting from the synergistic effect of transition metals, these trimetallic templates exhibit significantly superior fundamental OER performance compared to conventional mono-metal templates, with overpotentials between 280 and 400 mV at a current density of 10 mA cm^{-2}. Furthermore, by regulating the hydrothermal sulphuration time, ternary metal sulphide (FeNiZnS-1) is synthesized without destroying the original morphology of the FeNiZn template. FeNiZnS-1 exhibits a low overpotential of 249 mV to reach a current density of 10 mA cm^{-2}, with a Tafel slope of 41.4 mV dec^{-1}. Meanwhile, it also demonstrates remarkable electrochemical durability in the OER and overall water splitting.
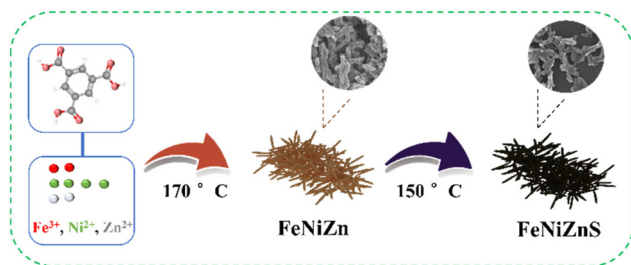
Results and discussion

As shown in Scheme 1, the MOF templates are synthesized *via* a convenient one-pot hydrothermal method. Various metal salts and 1,3,5-trimesic acid (H$_3$BTC) are dissolved in a DMF solution. The mixture undergoes a 24 h reaction at 170 °C in a Teflon-lined autoclave to yield the respective MOF templates.[30] The monometallic Fe-MIL100 formed by the coordination of Fe^{3+} and H$_3$BTC exhibits a polyhedral structure with octahedra.[31] When the Ni element is added into the reaction system, the bimetallic FeNi-MOF exhibits a topological structure similar to Fe-MIL100.[32] However, when the third transition element (M = Zn, Co or Cd) participates in the reaction system, the morphology of the trimetallic MOF undergoes a transform-

ation, forming a coral-like nanostructure (Fig. S1†). It can be observed that the slight differences in sizes of the three MOF templates can be ascribed to differences in the coordination abilities of various transition metals.[33,34]

The trimetallic FeNiZn template is transformed into the MOF-derived sulfide through hydrothermal sulfurization at 150 °C. According to the duration of sulfurization time, trimetallic sulfides can be divided into FeNiZnS-1, FeNiZnS-2, and FeNiZnS-3. As shown in Fig. S2,† the coral-like nanostructures of the trimetallic FeNiZn template are gradually destroyed with increasing sulfidation time, ultimately transforming into dispersed nanosulfides. By controlling the reaction time, conversion of sulfides and protection of the coral-like morphology can be achieved.

The morphological characterization of the FeNiZn template and FeNiZnS-1 is recorded and shown in Fig. 1. As shown in Fig. 1a and b, the ternary FeNiZn template exhibits a uniform coral-like morphology as expected. Good dispersibility allows the FeNiZn template to fully come in contact with the sulfur source during the vulcanization process. It can be easily observed that FeNiZnS-1 synthesized through 1 h hydrothermal sulfidation still retains a clear coral-like nanostructure (Fig. 1c and d). Similarly, the intricate coral-like stacking of FeNiZnS-1 is revealed through HAADF-STEM (Fig. S3a†). The crystallinity of the material is determined by high-resolution TEM. As shown in Fig. S3b,† no clear lattice fringes are
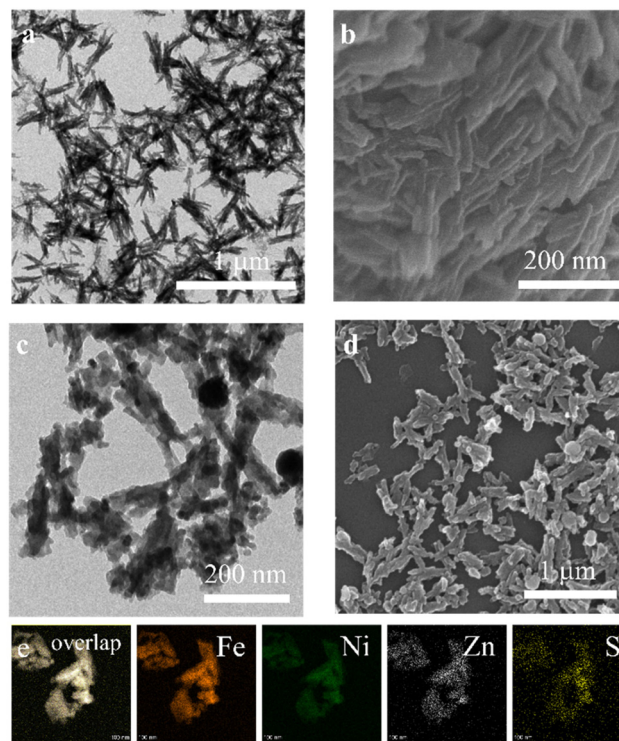

Fig. 1 Morphological characterization of FeNiZn and FeNiZnS-1: (a) TEM image of FeNiZn, (b) SEM image of FeNiZn, (c) TEM image of FeNiZnS-1, (d) SEM image of FeNiZnS-1, and (e) elemental mappings of FeNiZnS-1.

Scheme 1 The synthetic procedures of the trimetallic MOF template and FeNiZnS catalysts.

observed for FeNiZnS-1, indicating its amorphous structure. The long-range disordered amorphous structure of FeNiZnS-1 provides potential active sites for participating in catalytic reaction processes.[35] In addition, the EDS spectra of the trimetallic templates and sulfides reflect the elemental composition of the catalysts (Fig. S4 and S5†). The trimetallic templates and sulfides both manifest the anticipated elemental proportion, confirming the stable synthesis capability of this system. Furthermore, STEM-EDX elemental mapping is utilized to analyze the elemental composition and distribution of FeNiZnS-1. As depicted in Fig. 1e, FeNiZnS-1 exhibits a homogeneous elemental distribution of Fe, Ni, Zn and S, confirming the formation of trimetallic sulfides.

The XRD patterns depicted in Fig. 2a demonstrate a similar conclusion, consistent with the previous analysis. Apart from the derivative peaks attributed to MOFs themself, ternary metal sulfides did not exhibit distinct diffraction peaks, confirming the prior conclusions regarding the low crystallinity of FeNiZnS-1. The diffraction peaks of the FeNiZn template located at 10.54° and 25.34° gradually diminish with increasing sulfidation time, indicating the transformation of the pristine MOF. It is worth noting that the diffraction peaks located at 20.73° and 22.73° correspond to the (202) and (114) crystal planes of $NiSO_4·6H_2O$ (PDF#79-0189), and the peak at around 32.38° is assigned to the (200) crystal plane of $(FeNi)S_2$

(PDF#02-0850), respectively. This indicates that the generation of $NiSO_4·6H_2O$ and $(FeNi)S_2$ may be the primary factor leading to the collapse of the coral-like nanostructure.

Moreover, a series of X-ray photoelectron spectroscopy (XPS) tests are employed to assess the elemental valence of catalytic materials. Compared to the FeNiZn template, the FeNiZnS-1 catalyst exhibits a distinct S 2p peak in the survey scan, indicating the successful introduction of sulfur during the sulfidation process (Fig. 2b). Additionally, the constituent elements in FeNiZnS-1 have been thoroughly examined. As illustrated in Fig. 2c, the peaks located at 711.27 and 714.98 eV are matched with Fe $2p_{3/2}$ and Fe $2p_{1/2}$.[36] Notably, the Ni 2p spectrum of FeNiZnS-1 (Fig. 2d) displays characteristic peaks at 856.05, 860.87 and 853.08 eV, which correspond to Ni $2p_{3/2}$, Ni $2p_{1/2}$ and Ni[0].[37] In addition, in the high-resolution Zn 2p spectrum (Fig. 2e), the peaks found at 1022.08 and 1045.08 eV are attributed to Zn $2p_{3/2}$ and $2p_{1/2}$, respectively.[38] The S 2p XPS spectra of FeNiZnS-1 are depicted in Fig. 2f. The peaks observed at 162.2 and 163.5 are ascribed to S^{2-} $2p_{3/2}$ and S_2^{2-} $2p_{1/2}$ and S_2^{2-} $2p_{1/2}$, which correspond to the bond between the metal and sulfur, indicating the conversion of the MOF into metal sulfide.[39] Likewise, the characteristic peak at around 168.65 eV indicates the generation of S–O bonds in the FeNiZnS-1 sample when exposed to air.[40] Additionally, by testing samples with different degrees of sulphuration, we can explore changes in the valence states of each element during the reaction process (Fig. S6–S8†). As depicted in Fig. S9a,† the binding energy of Fe $2p_{3/2}$ and Ni $2p_{3/2}$ in FeNiZnS-1 leads to an upward shift, whereas the binding energy of Zn results in a negative shift. With increasing sulphuration time, the binding energies of Fe, Ni, and Zn elements exhibit a positive shift. In FeNiZnS-1, the valences of Fe and Ni species increase while those of Zn species decrease. Electron transfer occurs from Fe and Ni species to Zn species, confirming that sulfidation alters the electronic structure of the FeNiZn template.[41] In the S 2p energy level, the ratio of S–O to M–S peak areas increases with prolonged sulphuration time, thereby confirming conclusions drawn from XRD analysis regarding the formation of $NiSO_4·6H_2O$ species. So, through a detailed analysis of the morphological structure, elemental distribution, phases, and surface chemical environment of FeNiZnS-1, the successful synthesis of the FeNiZnS-1 catalyst can be clearly verified.

Relevant electrochemical experiments are conducted with a glassy carbon electrode as the working electrode in a 1 M KOH solution at room temperature. To prepare the catalyst ink, 3 mg of catalyst and 3 mg carbon black were dispersed in a solution containing 0.99 mL of ethanol and 10 μL of Nafion, followed by sonication for 30 min. The linear sweep voltammetry curves (LSVs) of common monometallic templates (ZIF8 and ZIF67) are recorded and shown in Fig. S10† to evaluate the enhancement of the OER activity of the trimetallic template compared to that of the monometallic template. ZIF8 and ZIF67 exhibit an unsatisfactory OER performance, requiring overpotentials of 412 and 510 mV to attain a current density of 10 mA cm^{-2}, respectively. As depicted in Fig. 3a and b, the FeNiZn, FeNiCo and FeNiCd templates possess an outstanding
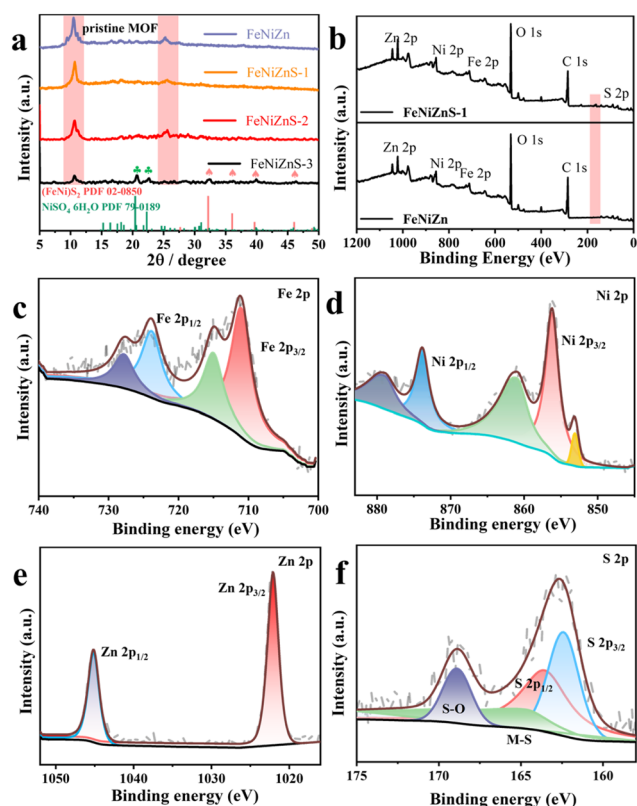

Fig. 2 (a) XRD patterns of FeNiZn, FeNiZnS-1, FeNiZnS-2, and FeNiZnS-3. XPS spectra of FeNiZnS-1, (b) survey scan, (c) Fe 2p, (d) Ni 2p, (e) Zn 2p and (f) S 2p.
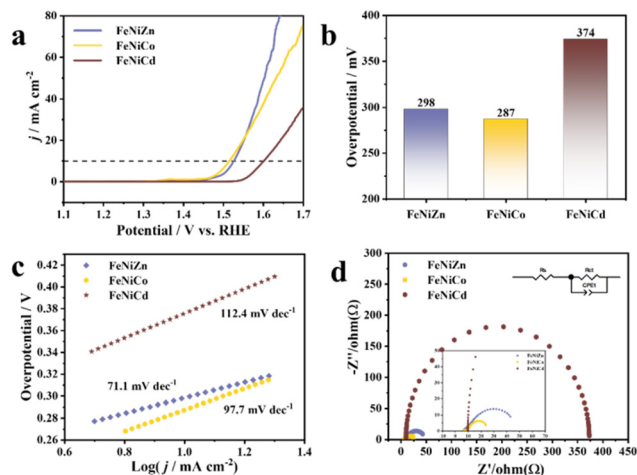
6066 | *Inorg. Chem. Front.*, 2024, **11**, 6064–6071

This journal is © the Partner Organisations 2024

Fig. 3 Electrochemical OER performance of trimetallic templates (FeNiZn, FeNiCo and FeNiCd). (a) LSV curves, (b) the corresponding overpotential histograms, (c) Tafel slope, and (d) EIS Nyquist plots.

electrocatalytic performance, with overpotentials of only 298, 287 and 374 mV at 10 mA cm^{-2}, significantly lower than those of the monometallic templates. This indicates that the metal sites of trimetallic catalysts and the synergistic effects of transition metal elements contribute additional efficacious active sites for the OER process, enhancing the overall catalytic performance of the material. Furthermore, in order to delve into the intrinsic activity of the trimetallic template, the data of the Tafel slope are determined by fitting the LSV at a scanning rate of 5 mV s^{-1} (Fig. 3c). The FeNiZn template exhibits a Tafel slope of 71.1 mV dec^{-1}, lower than those of FeNiCo (97.7 mV dec^{-1}) and FeNiCd (112.4 mV dec^{-1}) templates. The electrochemical impedance spectroscopy (EIS) plot reveals the charge transfer resistance of the trimetallic templates. FeNiCd exhibits a larger charge transfer resistance compared to FeNiZn and FeNiCo, which confirms that FeNiZn and FeNiCo have better performance due to their higher electron transfer efficiency in reactions (Fig. 3d and Table. S1†). Furthermore, the double layer capacitance (C_{dl}) value and electrochemically active surface area (ECSA) of the electrocatalysts are obtained through CV tests conducted at different scanning rates (10 mV s^{-1} to 50 mV s^{-1}). Similarly, the FeNiZn template exhibits the highest C_{dl} value (1.91 mF cm^{-2}) compared to FeNiCo (1.88 mF cm^{-2}) and FeNiCd (0.67 mF cm^{-2}), indicating the largest abundance of active sites during the electrochemical process (Fig. S11†). These electrochemical characterization results verify that the FeNiZn template possesses superior electronic transport capabilities, effective active surface area and catalytic kinetics compared to other trimetallic templates. We have conducted basal evaluations of the OER performance of two types of template sulfides (FeNiZnS and FeNiCoS). As shown in Fig. S12,† FeNiZnS exhibits better OER performance than its precursor, while FeNiCoS does not exhibit significant performance enhancement compared to the precursor. On the whole, the FeNiZn template is more suitable as a precursor for MOF-derived sulfides.

Thanks to the remarkable OER performance of the ternary FeNiZn template, a series of ternary sulfide electrocatalysts are synthesized through a one-step hydrothermal sulfidation at different reaction times (1–3 h). As shown in Fig. 4a, the FeNiZnS-1 electrocatalyst demonstrates the most favorable overpotential of 249 mV at 10 mA cm^{-2}, a reduction of 49 mV compared to that of the FeNiZn template. This indicates that the amorphous coral-like nanostructure of FeNiZnS-1 with rich active sites could reduce the activation energy barrier, enhancing the OER performance of electrocatalysts. With the time of sulfidation increasing, FeNiZnS-2 and FeNiZnS-3 show higher overpotentials of 271 mV and 324 mV to drive a current density of 10 mA cm^{-2} (Fig. 4b). The deterioration of performance is attributed to the disruption of the template's coral-like nanostructure, reduction of effective electron transfer pathways, and formation of inert NiSO$_4$·6H$_2$O, matching with previous XRD analysis results. The kinetic characteristics of FeNiZnS-1 and other electrocatalysts are investigated using the Tafel slope (Fig. 4c). The FeNiZnS-1 electrocatalyst exhibits a low Tafel slope of 41.45 mV dec^{-1}, which is obviously lower than those of FeNiZnS-2 (89.3 mV dec^{-1}), FeNiZnS-3 (114.2 mV dec^{-1}) and commercial RuO$_2$ (165.1 mV dec^{-1}), indicating the fastest OER kinetics mechanism. As shown in Fig. 4d, the EIS Nyquist diagrams are obtained across frequency values ranging from 100 kHz to 1 Hz and fitted with an equivalent
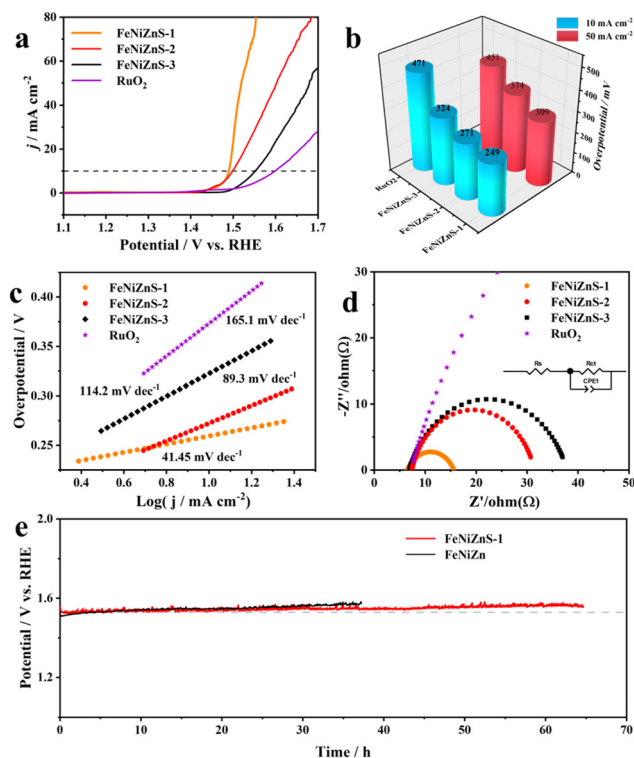

Fig. 4 Electrochemical performance and stability testes of trimetallic sulfides. (a) LSV curves of catalysts under different sulfidation times, (b) overpotential histograms, (c) Tafel slope fitted by LSV curves, (d) AC impedance test of FeNiZnS-1, FeNiZnS-2 and FeNiZnS-3, and (e) chronopotentiometry test at 10 cm^{-2}.

This journal is © the Partner Organisations 2024

Inorg. Chem. Front., 2024, **11**, 6064–6071 | **6067**

circuit model. FeNiZnS-1 displays a low charge transfer resistance (R_{ct}) of 9.14 Ω, which is lower than those of FeNiZnS-2 (15.12 Ω), FeNiZnS-3 (19.37 Ω) and commercial RuO₂ (120.8 Ω). The charge transfer resistance of trimetallic sulfides is significantly lower than that of the FeNiZn template, confirming that the sulfidation process significantly enhances the overall electrical conductivity of the materials, which is beneficial for charge transfer during the OER process. Similarly, the ECSA of trimetallic sulfides can be determined through the evaluation of the C_{dl} value (Fig. S13†). The FeNiZnS-1 electrocatalyst has a larger C_{dl} value (2.15 mF cm⁻²) than FeNiZnS-2 (1.19 mF cm⁻²) and FeNiZnS-3 (0.64 mF cm⁻²). Furthermore, the chronopotentiometry (CP) test is conducted to assess the stability of catalysts under a current density of 10 mA cm⁻² (Fig. 4e). FeNiZnS-1 shows remarkable long-term stability, exhibiting a negligible alteration in activity even after a duration of 60 h. In addition, the OER performance of FeNiZnS-1 is compared with that of metal sulfides and carbon black materials in recent years (Fig. S14 and Table S2†). It could be obviously observed that the FeNiZnS-1 catalysts outperform many kinds of previously reported sulfides and carbon black materials.

Moreover, in order to investigate deeply the electrocatalytic activity origins of trimetallic sulfides, a series of physical characterization studies and analyses are conducted on FeNiZnS-1 after the OER (FeNiZnS-1/AO). As depicted in Fig. 5a, it is obvious that when coupled with conductive carbon black, the trimetallic sulfides exhibit a surface covered with carbon black. HRTEM is employed for further examination of the relationship between carbon black and active species. The interlayer spacing of 0.38 nm is attributed to the result calculated using Bragg's law based on the (002) planes of carbon, confirming the successful loading of carbon black (Fig. S15†).[42] As shown in Fig. 5b and c, following electrochemical testing, a portion of the amorphous phase underwent crystalline transformation, resulting in the formation of an amorphous/crystalline interface.[43] The crystalline phase structure and carbon black fillers indeed enhanced the overall electrical conductivity of the material. Similarly, Fig. 5d illustrates two distinct lattice planes with interplanar spacings of 0.29 nm and 0.31 nm, corresponding to the (220) plane of FeOOH and the (110) plane of NiOOH.[44] The conductive carbon black possesses a high specific surface area capable of adsorbing the active species MOOH generated during the OER process, thereby preventing the aggregation of active species and the reduction of electrocatalytic activity.[45,46] Raman spectroscopy is used to assess alterations in the defect density of carbon materials during reaction processes (Fig. 5f). The D band and G band are located at 1350 cm⁻¹ and 1580 cm⁻¹ respectively, representing the degree of material defects and the stretching vibration mode of C sp² hybridization. The ratio (I_D/I_G) of FeNiZnS-1/AO shows an increasing trend compared to FeNiZnS-1, indicating that the carbon black and generation of active species promoted the overall electrocatalyst defectiveness.[47] XRD is used to investigate the phase composition of FeNiZnS-1/AO. The peak located at 25° is attributed to the (002) graphite-type reflections (Fig. S16†).[48] The absence of distinct diffraction peaks for hydroxylated oxides (MOOH) is due to
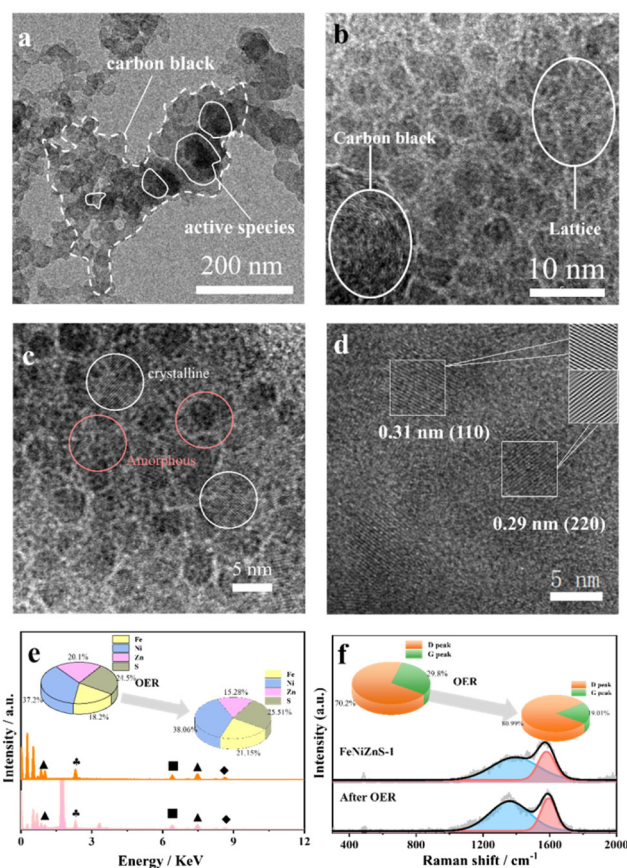

Fig. 5 The physical characterization images of FeNiZnS-1/AO: (a) TEM, (b, c and d) HRTEM, (e) SEM-EDS, and (f) Raman.

them being masked by the peaks of carbon black. The elemental surface compositions and chemical states of products after electrochemical tests are assessed. In the S 2p spectrum for FeNiZnS-1/AO (Fig. S17a†), the peaks of 2p₃/₂ and 2p₃/₂ exhibit a conspicuous diminution, indicating the transformation of metal sulfides into low-crystallinity (oxy)hydroxide during the anodic OER process. The augmentation of the S–O peak located at 168.7 eV is due to the oxidation of S species to SO₄²⁻ under high oxygenation conditions at the anode.[49] As illustrated in Fig. S16b,† the binding energy of Ni 2p₃/₂ and 2p₁/₂ has a slight upshift in comparison with that of FeNiZnS-1, suggesting the generation of active species with high oxidation states. The characteristic peak at 857.85 eV is attributed to Ni³⁺ of NiOOH.[50] Moreover, it is observed that there is an occurrence of zinc species dissolution during the transition from metal sulfides to (oxy)hydroxides (Fig. 5e). Finally, the d-band centers of trimetallic sulfides are measured based on high-resolution X-ray photoelectron spectroscopy (HR-XPS).[51,52] As shown in the diagram in Fig. S18,† the d-band center values of FeNiZn and FeNiZnS-1 are −7.71 and −7.38 eV, respectively. After sulfurization, the d-band center of FeNiZnS-1 becomes closer to the Fermi level, indicating enhanced interaction between the oxygen-containing intermediate and the catalyst surface.[53] In summary, FeNiZnS-1 exhibits excellent electrical conductivity
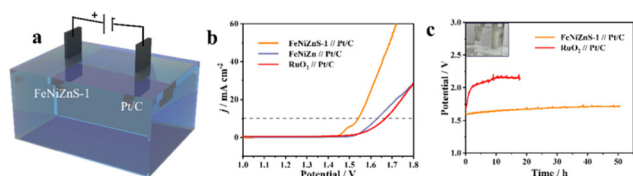
Fig. 6 (a) Schematic image, (b) LSV curves of FeNiZn//Pt/C, FeNiZnS-1//Pt/C and commercial RuO_2//Pt/C, and (c) CP test in alkaline solution.

and transforms into real time catalytic active species (MOOH) during the OER process, after coupling with carbon black. Benefiting from the preserved coral-like morphology and synergistic effects among transition metals, FeNiZnS-1 demonstrated outstanding OER catalytic potential as a pre-catalyst.

To evaluate the application prospects of electrocatalysts, we constructed a two-electrode system of FeNiZnS-1/Pt/C to drive overall water splitting in a 1 M KOH solution (Fig. 6a). The FeNiZnS-1//Pt/C electrode requires only 1.54 V to achieve a current density of 10 mA cm^{-2}, which is obviously lower than those of FeNiZn//Pt/C (1.63 V) and commercial RuO_2//Pt/C (1.67 V) electrodes (Fig. 6b). In addition, the electrochemical stability of FeNiZnS-1//Pt/C is evaluated through a long-term chronopotentiometry (CP) test at 10 mA cm^{-2}. As depicted in Fig. 6c, FeNiZnS-1//Pt/C exhibits a slight potential rise over a 50 h overall water splitting test, demonstrating excellent electrochemical stability compared to commercial RuO_2//Pt/C electrodes.

Conclusions

In summary, based on a facile hydrothermal method, we have synthesized a series of coral-like ternary MOF templates with similar morphologies. The further optimized FeNiZnS-1 has the following advantages during the OER process. (i) Benefiting from the synergistic effect of transition metals, the FeNiZn sacrificial template exhibits better OER activity than conventional mono-metal templates. (ii) Appropriate vulcanization time improves the electron transmission capability of the catalyst, while ensuring the integrity of the coral-like morphology. (iii) FeNiZnS-1 exhibits outstanding OER (overpotential of 249 mV at 10 mA cm^{-2}) and overall water splitting performance (1.54 V at 10 mA cm^{-2}). In addition, the real-time active species (NiOOH and FeOOH) in the OER are determined by analyzing the morphological changes, physical phases, and electronic structures of the post-reaction products. The synthesis method of high-performance multi-metal MOF templates and the FeNiZn MOF-derived sulfides in this work may offer insights for the development of efficient OER electrocatalysts.

Data availability

The data that support the findings of this study are available from the corresponding author, upon reasonable request.

Conflicts of interest

There are no conflicts to declare.

Acknowledgements

References

1 F. Gao, Y. Zhang, F. Ren, Y. Shiraishi and Y. Du, Universal surfactant-free strategy for self-standing 3D tremella-like Pd-M (M = Ag, Pb, and Au) nanosheets for superior alcohols electrocatalysis, *Adv. Funct. Mater.*, 2020, **30**(16), 2000255, DOI: **10.1002/adfm.202000255**.

2 J. Li, Y. Xu, C. Wang, Z. Wu, Y. Shiraishi and Y. Du, Interfacial engineering of platinum group metals electrocatalysts for advanced electrocatalysis, *Surf. Interfaces*, 2023, **42**, 103360, DOI: **10.1016/j.surfin.2023.103360**.

3 J. H. Kim, D. Hansora, P. Sharma, J.-W. Jang and J. S. Lee, Toward practical solar hydrogen production an artificial photosynthetic leaf-to-farm challenge, *Chem. Soc. Rev.*, 2019, **48**(7), 1908–1971, DOI: **10.1039/c8cs00699g**.

4 A. Odenweller, F. Ueckerdt, G. F. Nemet, M. Jensterle and G. Luderer, Probabilistic feasibility space of scaling up green hydrogen supply, *Nat. Energy*, 2022, **7**(9), 854–865, DOI: **10.1038/s41560-022-01097-4**.

5 Y. Ji, L. Yang, X. Ren, G. Cui, X. Xiong and X. Sun, Full water splitting electrocatalyzed by $NiWO_4$ nanowire array, *ACS Sustainable Chem. Eng.*, 2018, **6**(8), 9555–9559, DOI: **10.1021/acssuschemeng.8b01841**.

6 C. Bie, L. Wang and J. Yu, Challenges for photocatalytic overall water splitting, *Chem*, 2022, **8**(6), 1567–1574, DOI: **10.1016/j.chempr.2022.04.013**.

7 Q. Sun, Y. Tong, P. Chen, B. Zhou and X. Dong, Universal strategy of bimetal heterostructures as superior bifunctional catalysts for electrochemical water splitting, *ACS Sustainable Chem. Eng.*, 2021, **9**(11), 4206–4212, DOI: **10.1021/acssuschemeng.1c00037**.

8 Y. Zhang, X. Zheng, X. Guo, J. Zhang, A. Yuan, Y. Du and F. Gao, Design of modified MOFs electrocatalysts for water splitting: High current density operation and long-term stability, *Appl. Catal., B*, 2023, **336**, 122891, DOI: **10.1016/j.apcatb.2023.122891**.

9 Y. Tian, Z. Lin, J. Yu, S. Zhao, Q. Liu, J. Liu, R. Chen, Y. Qi, H. Zhang, R. Li, J. Li and J. Wang, Superaerophobic quaternary Ni–Co–S–P nanoparticles for efficient overall water-splitting, *ACS Sustainable Chem. Eng.*, 2019, 7(17), 14639–14646, DOI: **10.1021/acssuschemeng.9b02556**.

10 F. Gao, Y. Zhang, Z. Wu, H. You and Y. Du, Universal strategies to multi-dimensional noble-metal-based catalysts for electrocatalysis, *Coord. Chem. Rev.*, 2021, **436**, 213825, DOI: **10.1016/j.ccr.2021.213825**.

This journal is © the Partner Organisations 2024

Inorg. Chem. Front., 2024, **11**, 6064–6071 | **6069**

11 Y.-R. Hong, S. Dutta, S. W. Jang, O. F. Ngome Okello, H. Im, S.-Y. Choi, J. W. Han and I. S. Lee, Crystal facet-manipulated 2D Pt nano dendrites to achieve an intimate heterointerface for hydrogen evolution reactions, *J. Am. Chem. Soc.*, 2022, **144**(20), 9033–9043, DOI: **10.1021/jacs.2c01589**.

12 M.-L. Hu, M. Y. Masoomi and A. Morsali, Template strategies with MOFs, *Coord. Chem. Rev.*, 2019, **387**, 415–435, DOI: **10.1016/j.ccr.2019.02.021**.

13 B. Zhang, Y. Zheng, T. Ma, C. Yang, Y. Peng, Z. Zhou, M. Zhou, S. Li, Y. Wang and C. Cheng, Designing MOF nanoarchitectures for electrochemical water splitting, *Adv. Mater.*, 2021, **33**(17), 2006042, DOI: **10.1002/adma.202006042**.

14 K. Jayaramulu, S. Mukherjee, D. M. Morales, D. P. Dubal, A. K. Nanjundan, A. Schneemann, J. Masa, S. Kment, W. Schuhmann, M. Otyepka, R. Zbořil and R. A. Fischer, Graphene-based metal–organic framework hybrids for applications in catalysis, environmental, and energy technologies, *Chem. Rev.*, 2022, **122**(24), 17241–17338, DOI: **10.1021/acs.chemrev.2c00270**.

15 G. Gao, X. Chen, L. Han, G. Zhu, J. Jia, A. Cabot and Z. Sun, Advances in MOFs and their derivatives for non-noble metal electrocatalysts in water splitting, *Coord. Chem. Rev.*, 2024, **503**, 215639, DOI: **10.1016/j.ccr.2023.215639**.

16 Q. Wang and D. Astruc, State of the art and prospects in metal-organic framework (MOF)-based and MOF-derived nano catalysis, *Chem. Rev.*, 2020, **120**(2), 1438–1511, DOI: **10.1021/acs.chemrev.9b00223**.

17 D. Senthil Raja, X. F. Chuah and S. Y. Lu, In situ grown bi-metallic MOF-based composite as highly efficient bifunctional electrocatalyst for overall water splitting with ultra-stability at high current densities, *Adv. Energy Mater.*, 2018, **8**(23), 1801065, DOI: **10.1002/aenm.201801065**.

18 Q. Wang, H. Xu, X. Qian, G. He and H. Chen, Oxygen and sulphur dual vacancy engineering on a 3D Co_3O_4/Co_3S_4 heterostructure to improve overall water splitting activity, *Green Chem.*, 2022, **24**(23), 9220–9232, DOI: **10.1039/d2gc03315a**.

19 L. Chen, J.-T. Ren and Z.-Y. Yuan, Design strategies of phosphorus-containing catalysts for photocatalytic, photoelectrochemical and electrocatalytic water splitting, *Green Chem.*, 2022, **24**(2), 713–747, DOI: **10.1039/d1gc03768d**.

20 H. S. Jadhav, H. A. Bandal, S. Ramakrishna and H. Kim, Critical review, recent updates on zeolitic imidazolate framework-67 (ZIF-67) and its derivatives for electro-chemical water splitting, *Adv. Mater.*, 2022, **34**(11), e2107072, DOI: **10.1002/adma.202107072**.

21 M. Zhang, Q. Dai, H. Zheng, M. Chen and L. Dai, Novel MOF-derived Co@N-C bifunctional catalysts for highly efficient Zn-air batteries and water splitting, *Adv. Mater.*, 2018, **30**(10), 1705431, DOI: **10.1002/adma.201705431**.

22 J. Shi, F. Qiu, W. Yuan, M. Guo and Z.-H. Lu, Nitrogen-doped carbon-decorated yolk-shell CoP@FeCoP micro-poly-hedral derived from MOF for efficient overall water splitting, *Chem. Eng. J.*, 2021, **403**, 126312, DOI: **10.1016/j.cej.2020.126312**.

23 X. Zhao, H. Liu, Y. Rao, X. Li, J. Wang, G. Xia and M. Wu, Carbon dots decorated hierarchical $NiCo_2S_4/Ni_3S_2$ composite for efficient water splitting, *ACS Sustainable Chem. Eng.*, 2018, **7**(2), 2610–2618, DOI: **10.1021/acssuschemeng.8b05611**.

24 A. Hameed, M. Batool, Z. Liu, M. A. Nadeem and R. Jin, Layered double hydroxide-derived nanomaterials for efficient electrocatalytic water splitting: Recent progress and future perspective, *ACS Energy Lett.*, 2022, **7**(10), 3311–3328, DOI: **10.1021/acsenergylett.2c01362**.

25 S. Li, L. Tong, Z. Peng, B. Zhang and X. Fu, A novel high-entropy sulfide $(ZnCoMMnFeAlMg)_9S_8$ as a low potential and long life electrocatalyst for overall water splitting in experiments and DFT analysis, *Green Chem.*, 2024, **26**(1), 384–395, DOI: **10.1039/d3gc03800a**.

26 Y. Shi, B. Zhu, X. Guo, W. Li, W. Ma, X. Wu and H. Pang, MOF-derived metal sulfides for electrochemical energy applications, *Energy Storage Mater.*, 2022, **51**, 840–872, DOI: **10.1016/j.ensm.2022.07.027**.

27 Y. Zhang, F. Gao, D. Wang, Z. Li, X. Wang, C. Wang, K. Zhang and Y. Du, Amorphous/crystalline heterostructure transition-metal-based catalysts for high-performance water splitting, *Coord. Chem. Rev.*, 2023, **475**, 214916, DOI: **10.1016/j.ccr.2022.214916**.

28 H. Hu, Z. Wang, L. Cao, L. Zeng, C. Zhang, W. Lin and C. Wang, Metal–organic frameworks embedded in a lipo-some facilitate overall photocatalytic water splitting, *Nat. Chem.*, 2021, **13**(4), 358–366, DOI: **10.1038/s41557-020-00635-5**.

29 G. Cai, W. Zhang, L. Jiao, S.-H. Yu and H.-L. Jiang, Template-directed growth of well-aligned MOF arrays and derived self-supporting electrodes for water splitting, *Chem*, 2017, **2**(6), 791–802, DOI: **10.1016/j.chempr.2017.04.016**.

30 T. Liu, Y. Zhang, C. Ye, D. Wang, C. Wang and Y. Du, Component regulation on ternary FeCoNi nano-bundles as efficient electrocatalysts for driving water oxidation, *J. Colloid Interface Sci.*, 2024, **655**, 466–473, DOI: **10.1016/j.jcis.2023.11.029**.

31 M. Ahmad, S. Chen, F. Ye, X. Quan, S. Afzal, H. Yu and X. Zhao, Efficient photo-Fenton activity in mesoporous MIL-100(Fe) decorated with ZnO nanosphere for pollutants degradation, *Appl. Catal. B*, 2019, **245**, 428–438, DOI: **10.1016/j.apcatb.2018.12.057**.

32 F. Zheng, Z. Zhang, D. Xiang, P. Li, C. Du, Z. Zhuang, X. Li and W. Chen, Fe/Ni bimetal organic framework as efficient oxygen evolution catalyst with low overpotential, *J. Colloid Interface Sci.*, 2019, **555**, 541–547, DOI: **10.1016/j.jcis.2019.08.005**.

33 W. Li, X. Guo, P. Geng, M. Du, Q. Jing, X. Chen, G. Zhang, H. Li, Q. Xu, P. Braunstein and H. Pang, Rational design and general synthesis of multi-metallic metal-organic framework nano-octahedra for enhanced Li-S battery, *Adv. Mater.*, 2021, **33**(45), e2105163, DOI: **10.1002/adma.202105163**.

6070 | *Inorg. Chem. Front.*, 2024, **11**, 6064–6071

This journal is © the Partner Organisations 2024

34 S. J. Patil, N. R. Chodankar, S.-K. Hwang, P. A. Shinde, G. Seeta Rama Raju, K. Shanmugam Ranjith, Y. S. Huh and Y.-K. Han, Co-metal–organic framework derived CoSe$_2$@MoSe$_2$ core–shell structure on carbon cloth as an efficient bifunctional catalyst for overall water splitting, *Chem. Eng. J.*, 2022, **429**, 132379, DOI: **10.1016/j.cej.2021.132379**.

35 B. Jia, B. Zhang, Z. Cai, X. Yang, L. Li and L. Guo, Construction of amorphous/crystalline heterointerfaces for enhanced electrochemical processes, *eScience*, 2023, **3**(2), 100112, DOI: **10.1016/j.esci.2023.100112**.

36 Q. Liu, Q. Su, W. Cheng, J. Ding, W. Zhang, J. Wang, Y. Wang, X. Wang and Y. Huang, Dual role of Fe boost lattice oxygen oxidation of Mo-based materials from kinetics and thermodynamics, *Appl. Catal. B*, 2024, **340**, 123188, DOI: **10.1016/j.apcatb.2023.123188**.

37 K. Chang, D. T. Tran, J. Wang, K. Dong, S. Prabhakaran, D. H. Kim, N. H. Kim and J. H. Lee, Triphasic Ni$_2$P−Fe$_2$P−CoP heterostructure interfaces for efficient overall water splitting powered by solar energy, *Appl. Catal. B*, 2023, **338**, 123016, DOI: **10.1016/j.apcatb.2023.123016**.

38 Y. Yang, H. Yao, Z. Yu, S. M. Islam, H. He, M. Yuan, Y. Yue, K. Xu, W. Hao, G. Sun, H. Li, S. Ma, P. Zapol and M. G. Kanatzidis, Hierarchical nano assembly of MoS$_2$/Co$_9$S$_8$/Ni$_3$S$_2$/Ni as a highly efficient electrocatalyst for overall water splitting in a wide pH range, *J. Am. Chem. Soc.*, 2019, **141**(26), 10417–10430, DOI: **10.1021/jacs.9b04492**.

39 T. Bao, Y. Xia, J. Lu, C. Zhang, J. Wang, L. Yuan, Y. Zhang, C. Liu and C. Yu, A pacman-like titanium-doped cobalt sulfide hollow superstructure for electrocatalytic oxygen evolution, *Small*, 2021, **18**(4), 2103106, DOI: **10.1002/smll.202103106**.

40 G. F. Chen, T. Y. Ma, Z. Q. Liu, N. Li, Y. Z. Su, K. Davey and S. Z. Qiao, Efficient and stable bifunctional electrocatalysts Ni/Ni$_x$M$_y$ (M = P, S) for overall water splitting, *Adv. Funct. Mater.*, 2016, **26**(19), 3314–3323, DOI: **10.1002/adfm.201505626**.

41 C. Chen, Y. Tuo, Q. Lu, H. Lu, S. Zhang, Y. Zhou, J. Zhang, Z. Liu, Z. Kang, X. Feng and D. Chen, Hierarchical trimetallic Co-Ni-Fe oxides derived from core-shell structured metal-organic frameworks for highly efficient oxygen evolution reaction, *Appl. Catal. B*, 2021, **287**, 119953, DOI: **10.1016/j.apcatb.2021.119953**.

42 R. Wang, J. Liu, J. Xie, Z. Cai, Y. Yu, Z. Zhang, X. Meng, C. Wang, X. Xu and J. Zou, Hollow nanocage with skeleton Ni-Fe sulfides modified by N-doped carbon quantum dots for enhancing mass transfer for oxygen electrocatalysis in zinc-air battery, *Appl. Catal. B*, 2023, **324**, 122230, DOI: **10.1016/j.apcatb.2022.122230**.

43 J. Wu, T. Yang, R. Fu, M. Zhou, L. Xia, Z. Wang and Y. Zhao, Constructing electrocatalysts with composition gradient distribution by solubility product theory:

44 X. Dou, D. Yuan, X. Liang, K. Song, R. Hu, L. Zhang, J. C. Roy, X. Jiang, H. K. Liu, Y. Dou and L. Yu, Synergy between Mo dopants and Ni vacancies in NiOOH for enhanced oxygen evolution reaction, *Chem. Eng. J.*, 2023, **468**, 143715, DOI: **10.1016/j.cej.2023.143715**.

45 Z. Wang, Y. Wang, N. Zhang, L. Ma, J. Sun, C. Yu, S. Liu and R. Jiang, Highly efficient oxygen evolution catalysis achieved by NiFe oxyhydroxide clusters anchored on carbon black, *J. Mater. Chem. A*, 2022, **10**(19), 10342–10349, DOI: **10.1039/d2ta01931k**.

46 W. Ou, X. Ye and Y. Zhou, Recent advances in Ni (oxy) hydroxides and Ni sulfides catalysts for oxygen evolution reactions, *Coord. Chem. Rev.*, 2023, **493**, 215274, DOI: **10.1016/j.ccr.2023.215274**.

47 W. S. Jung and B. N. Popov, Improved durability of Pt catalyst supported on N-doped mesoporous graphitized carbon for oxygen reduction reaction in polymer electrolyte membrane fuel cells, *Carbon*, 2017, **122**, 746–755, DOI: **10.1016/j.carbon.2017.07.028**.

48 A. Al Sheikh Omar, F. M. Salehi, M. Bai, B. J. Inkson and A. Morina, In situ nanocompression of carbon black to understand the tribology of contaminated diesel engine oils, *Carbon*, 2023, **212**, 118170, DOI: **10.1016/j.carbon.2023.118170**.

49 T. G. Yun, Y. Sim, Y. Lim, D. Kim, J.-S. An, H. Lee, Y. Du and S.-Y. Chung, Surface dissolution and amorphization of electrocatalysts during oxygen evolution reaction: Atomistic features and viewpoints, *Mater. Today*, 2022, **58**, 221–237, DOI: **10.1016/j.mattod.2022.06.023**.

50 Q. Xu, H. Jiang, H. Zhang, Y. Hu and C. Li, Heterogeneous interface engineered atomic configuration on ultrathin Ni (OH)$_2$/Ni$_3$S$_2$ nanoforests for efficient water splitting, *Appl. Catal. B*, 2019, **242**, 60–66, DOI: **10.1016/j.apcatb.2018.09.064**.

51 S. J. Hwang, S.-K. Kim, J.-G. Lee, S.-C. Lee, J. H. Jang, P. Kim, T.-H. Lim, Y.-E. Sung and S. J. Yoo, Role of electronic perturbation in stability and activity of Pt-based alloy nanocatalysts for oxygen reduction, *J. Am. Chem. Soc.*, 2012, **134**(48), 19508–19511, DOI: **10.1021/ja307951y**.

52 S. Hu, F. Munoz, J. Noborikawa, J. Haan, L. Scudiero and S. Ha, Carbon supported Pd-based bimetallic and trimetallic catalyst for formic acid electrochemical oxidation, *Appl. Catal. B*, 2016, **180**, 758–765, DOI: **10.1016/j.apcatb.2015.07.023**.

53 Y. Tang, K. Shen, J. Zheng, B. He, J. Chen, J. Lu, W. Ge, L. Shen, P. Yang and S. Deng, D-band center modulating of CoO$_x$/Co$_9$S$_8$ by oxygen vacancies for fast-kinetics pathway of water oxidation, *Chem. Eng. J.*, 2022, **427**, 130915, DOI: **10.1016/j.cej.2021.130915**.

Amorphous/crystalline CoNiFe-LDH; hollow nanocages, *Adv. Funct. Mater.*, 2023, **33**(37), 2300808, DOI: **10.1002/adfm.202300808**.